

# Gold-Aptamer-Modified Metal–Organic Framework Drug Delivery Nanosystems for Combined Photothermal/Chemotherapy of Cancer

Ting Fang, Zihao Duan, Nan Wan, Xiaoxuan Zuo, Zhongwu Pan, Weiwei Zhang,\* Fei Ge,\* and Lin Gui\*



Cite This: *ACS Appl. Nano Mater.* 2024, 7, 12129–12141



Read Online

ACCESS |



Metrics & More



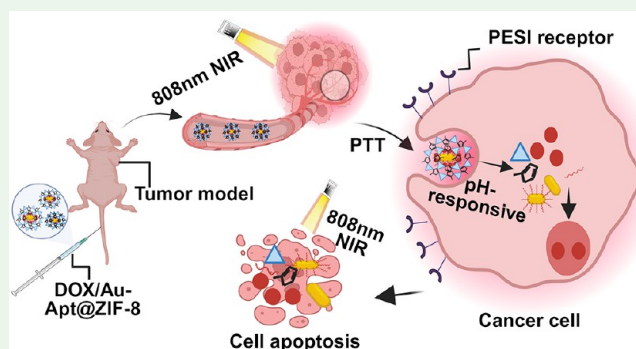
Article Recommendations



Supporting Information

**ABSTRACT:** The poor targeting and high toxicity of chemotherapeutic drugs make them less effective against breast cancer. In this study, in accordance with their photothermal effect, the aptamer (Apt) (AS1411) and doxorubicin (DOX) were linked to zeolite imidazole salt frame8 (ZIF-8) by using gold nanorods (Au NRs). Thereby, a multifunctional targeting nanoparticle platform (DOX/Au-Apt@ZIF-8) was constructed to deliver and effectively utilize DOX and realize the antitumor effects of the multimodal combination of chemotherapy–target–photothermal therapy. This platform was responsive to both pH and near-infrared (NIR) light. In the characterization experiments, DOX/Au-Apt@ZIF-8 exhibited good dispersibility, particle size stability, and consistent spectral characteristics. The photothermal conversion efficiency was up to 53.5%. In the cell uptake and cell cycle experiments, DOX/Au-Apt@ZIF-8 effectively targeted tumor cells and blocked their growth in the S phase. Moreover, in an *in vivo* study, DOX/Au-Apt@ZIF-8 exerted good inhibitory effects and photothermal effects on tumors. When combined with NIR irradiation, DOX/Au-Apt@ZIF-8 inhibited tumor tissue growth by enhancing and inducing apoptosis. Importantly, histopathological analysis revealed that the nanoparticles were less toxic to other organs and had high biosafety. As such, DOX/Au-Apt@ZIF-8 fabricated in this study is expected to offer a treatment approach against breast cancer.

**KEYWORDS:** Au NRs, nanotechnology, pH-responsive, targeted/photothermal therapy, combination antitumor



## INTRODUCTION

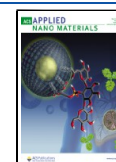
Currently, breast cancer remains one of the most common cancers, with the highest incidence and mortality, affecting women worldwide. It severely affects the quality of life and health of women.<sup>1–3</sup> For a long time, chemotherapy has been the main treatment method.<sup>4</sup> However, conventional chemotherapy drugs usually involve systemic toxicity, which causes a great extent of damage to the normal cells.<sup>5,6</sup> Therefore, the development of multifunctional nanodrug delivery system is of much interest.<sup>7</sup>

The metal–organic frame material the zeolite imidazolate frame (ZIF), which has good thermal stability, a large aperture, and a large surface area, is frequently employed in support design.<sup>8,9</sup> ZIF-8, a representative of the ZIF family, is a type of pH-responsive metal–organic framework.<sup>10</sup> When ZIF-8 enters the tumor microenvironment characterized by a low pH value, its skeleton collapses, which, in turn, increases the speed of drug release. The collapsed skeleton is used by the organism, which then greatly reduces the harm incurred to the body. Qian<sup>11</sup> designed and synthesized injectable polysaccharide hydrogel-supported copper sulfide and pH-responsive DOX@ZIF-8 nanoparticles. DOX@ZIF-8 can decompose in an acidic intracellular environment, achieve controlled DOX

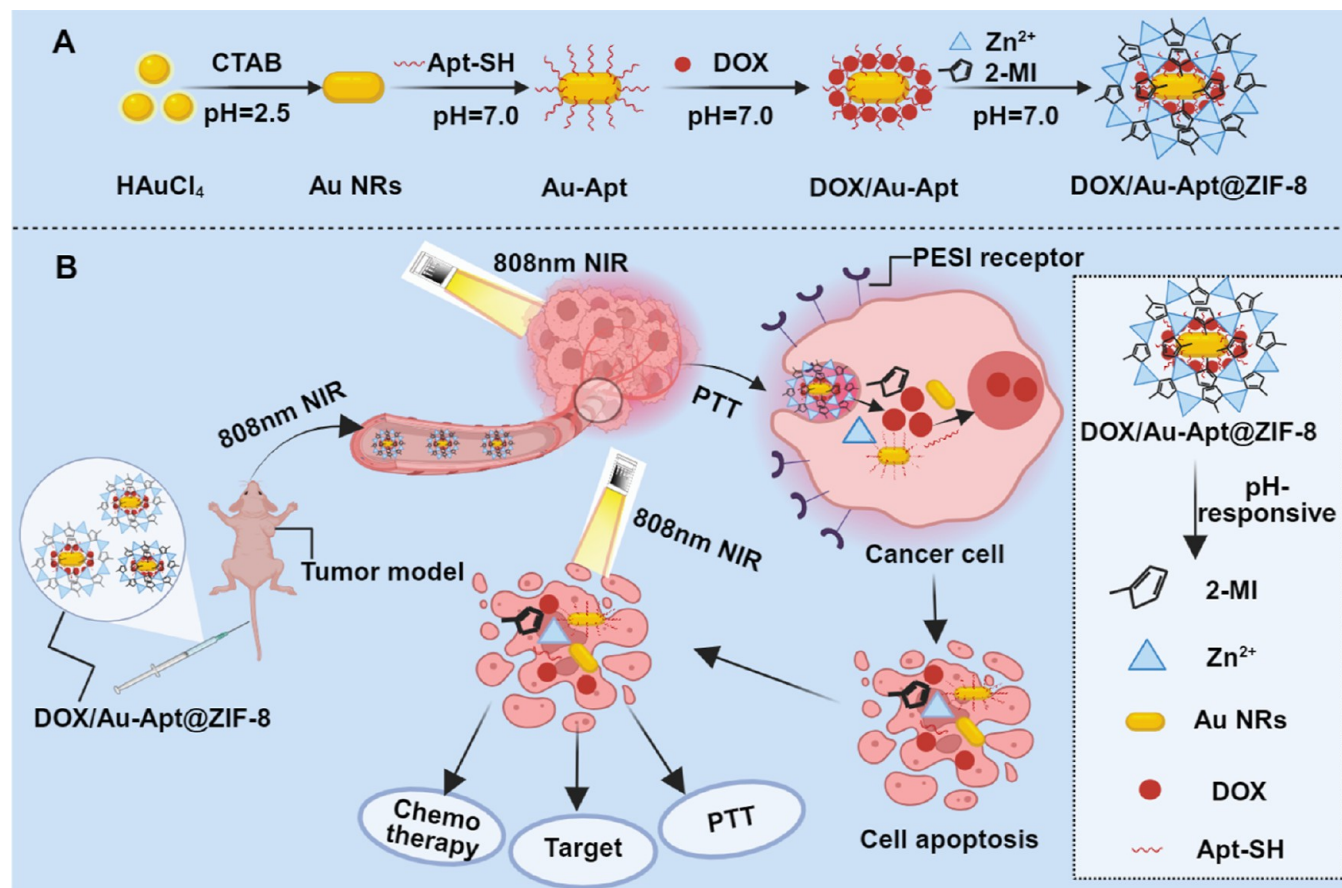
release, and help achieve photothermal-photodynamic treatment of cancer. Peng<sup>12</sup> encapsulated HF in ZIF-8 and optimized the drug-carrying complex PEG/ZIF-8@HF with a high encapsulation rate of 92.12% by using polyethylene glycol (PEG-2000). This drug delivery system exhibited selective drug release in an acidic microenvironment, thereby offering an effective treatment strategy for melanoma.

Although nanoparticles can wrap chemotherapy drugs and deliver them to the tumor tissues, the nanoparticles themselves are not specific to tumor cells.<sup>13</sup> The preferential accumulation of nanoparticles at tumor sites is attributed to the enhanced permeability and retention (EPR) effect of the tumor tissues.<sup>14,15</sup> To achieve specific targeting of chemotherapeutic drugs to the tumor sites, the development of targeted nanomedicine delivery systems has become a prominent area of research.<sup>16</sup> AS1411 is a nucleoprotein-targeted DNA

**Received:** April 9, 2024  
**Revised:** April 21, 2024  
**Accepted:** April 26, 2024  
**Published:** May 7, 2024



**Scheme 1. Synthesis and Working Principle of DOX/Au-Apt@ZIF-8 Nanoparticles; (A) Schematic Representation of the Synthesis of DOX/Au-Apt@ZIF-8 Nanoparticles; (B) Therapeutic Mechanisms of DOX/Au-Apt@ZIF-8 in the Development of a Targeted Nanodrug Delivery System and the Multimodal Combination of Chemotherapy–Target–PTT for Antitumor Applications**



aptamer (Apt) with low immunogenicity and production costs, high batch reproducibility and temperature stability, high affinity for tumor cells, and an ability to actively target tumor cells.<sup>17–22</sup> Previous literature has demonstrated that albumin, mesoporous silica, Au NRs, and other nanocarriers can obtain good targeting ability after being modified with an AS1411 Apt.<sup>17,18,23</sup> Yaghoobi<sup>24</sup> synthesized a linear DNA nanostructure to target Epi and anti-miR-10b in tumor cells. The combination of FOXM1-Apt, Epi, anti-miR-10b, and AS1411-Apt allowed the vector to selectively detect and treat cancer cells with positive nucleoli. The nanodrug delivery system can effectively and selectively deliver chemotherapy drugs to tumor cells so as to realize effective antitumor applications.

Presently, combination therapy is widely used to improve therapeutic efficacy.<sup>25</sup> As such, the introduction of photothermal therapy (PTT) provides a more effective treatment strategy to further improve the antitumor effect of nanodrug delivery systems. This treatment strategy is safe, noninvasive, and operable,<sup>26</sup> and NIR irradiation can activate photosensitizers to generate heat, which directly kills cancer cells or increases their sensitivity to chemotherapy, thereby reducing the drug dose or overcoming multidrug resistance.<sup>27,28</sup> NIR irradiation offers the advantages of low tissue absorption, negligible scattering, and deep penetration,<sup>29</sup> which can control local PTT-induced hyperthermia when combined with chemotherapeutic drugs and reduce the drug side effects.<sup>30</sup> The commonly used organic and inorganic nano-

particles with NIR absorption include gold nanorods (Au NRs), indocyanine green, graphene oxide, and hollow copper sulfide nanoparticles.<sup>31–34</sup> Gold nanoparticles of different forms have been extensively used in PTT and have been found to exert significant antitumor effects.<sup>35,36</sup> Hao<sup>37</sup> synthesized tetrahedral DNA nanostructured modified Au NRs nanocomposites (GNR@TDN-DOX). The nanocomposite exhibited high photothermal conversion performance under 808 nm NIR irradiation, thereby achieving effective antitumor effects.

Therefore, AS1411 was used in the present study to modify Au NRs and ZIF-8 in order to build a cancer drug delivery system (DOX/Au-Apt@ZIF-8), which offers the advantages of small size, high drug loading capacity, good biocompatibility, good photothermal performance, and target specificity. Meanwhile, due to the pH response of ZIF-8, the nanoparticle can realize the slow and controlled release of chemotherapy drugs in the tumor microenvironment and promote the accumulation of more chemotherapy drugs (DOX) and photothermal materials (Au NRs) at the tumor site under the dual passive and active targeting caused by the EPR effect and Apt, which then improve the bioavailability of drugs and the photothermal effect of nanomaterials so as to effectively strengthen the antitumor effect of nanomaterials while reducing the side effects of the drugs. The prepared DOX/Au-Apt@ZIF-8 was characterized and its drug release rates at different pH were analyzed. Moreover, the antitumor effects and the targeting of

DOX/Au-Apt@ZIF-8 combined with PTT were verified through *in vivo* and animal experiments, thereby offering a theoretical and experimental basis for further developing a targeted nanodrug delivery system and the multimodal combination of chemotherapy–target–PTT for their anti-tumor applications (Scheme 1).

## EXPERIMENTAL SECTION

**Materials.** HAuCl<sub>4</sub>·3H<sub>2</sub>O (≥99.9%), sodium borohydride (NaBH<sub>4</sub>), HCl (37%), silver nitrate (AgNO<sub>3</sub>), tri(2-carboxyethyl)-phosphine hydrochloride, 2-methylimidazole, zinc nitrate hexahydrate, cetyltrimethylammonium bromide (CTAB), and polyvinylpyrrolidone (PVP, wt 40,000) were purchased from Aladdin Chemical Reagents Co., Ltd. (Hefei, China). The AS1411 DNA Apt modified with a disulfide bond was synthesized by Jinsilui Biotechnology Co., Ltd. (Hefei, China). MCF-7 cells were purchased from Secu Biotechnology Co., Ltd. (Guangzhou, China).

**Synthesis of Au NRs.** Based on previous literature, Au NRs were synthesized using the seed growth method.<sup>38</sup> First, 500 μL of HAuCl<sub>4</sub> (0.01 M) was mixed with 10 mL of CTAB (0.2 M), and 1.2 mL of NaBH<sub>4</sub> (0.01 M) was then added quickly during stirring. After the mixture was stirred for 2 min, it was left in a constant temperature water bath at 30 °C for 2 h. Second, 100 mL of CTAB (0.2 M) and 10 mL of HAuCl<sub>4</sub> (0.01 M) were mixed, and then 3 mL of AgNO<sub>3</sub> (0.01 M) was added. After this mixture was gently mixed, 1.3 mL of HCl (0.1 M) was added to prepare the growth solution. Finally, 240 μL of the gold seed solution was added to this growth solution, which was then placed in a constant temperature water bath at 30 °C overnight. The newly prepared Au NR solution was centrifuged (8000 rpm, 10 min), and the precipitate was collected. CTAB in the solution was removed by washing thrice with ultrapure water.

**Synthesis of Au-Apt.** The experiment employed 5'-end thiol-modified oligonucleotides, specifically the single-stranded nucleic acid aptamer AS1411, which was purchased from Shanghai Aladdin Biochemical Co., Ltd. The synthetic sequence used is as follows:

5'-S-S-A A A A A A-G G T G G T G G T G G T T G T G G T G G T G G T G G

The disulfide bond of the Apt was initially cleaved by tri(2-carboxyethyl)phosphine hydrochloride, thereby exposing the sulfhydryl group. After cracking for 30 min, the Apt (100 μL, 100 μM) was then added to Au NRs (10 mL, 5 nM) and incubated overnight for self-assembly to form Au-Apt.<sup>39</sup>

**Synthesis of DOX/Au-Apt@ZIF-8.** DOX/Au-Apt@ZIF-8 was synthesized from DOX and Au-Apt@ZIF-8 by the methods of 1:2, 1:1, and 2:1. The synthesis method of DOX/Au-Apt@ZIF-8 using the 1:1 method is described here as an example: first, 0.02 g of PVP was added to 2 mL of the prepared Au NR solution and mixed evenly, and the PVP–Au NR solution was obtained after stirring away from light for 1 h. Then, 10 mg of DOX was added, and the solution was mixed evenly, followed by adjusting the pH of the solution to 7.0 and continuing to stir away from light for 1 h. Then, 5 mg of DOX was added to the solution and mixed evenly, followed by continuous stirring for 1 h. Then, 0.01 g of Zn(NO<sub>3</sub>)<sub>6</sub>H<sub>2</sub>O was dissolved in 5 mL of the methanol solution and added to the DOX/Au-Apt solution for 1 h and stirred without light to fix Zn<sup>2+</sup>. Then, 0.02 g of 2-methylimidazole was dissolved in 10 mL of the methanol solution and added to the above-mentioned solution. After stirring without light for 24 h, the mixture was centrifuged at 10,000 rpm for 10 min. The precipitate was collected and washed thrice with ethanol.<sup>40</sup>

**Characterization of DOX/Au-Apt@ZIF-8.** An AS-4800 scanning electron microscope (Hitachi, Japan) and FEI-TALOS-F200X transmission electron microscopy (Thermo Fisher, USA) were used to observe the morphologies of Au NRs and DOX/Au-Apt@ZIF-8, respectively. The optical properties and size of DOX/Au-Apt@ZIF-8 were characterized through dynamic light scattering (DLS), and its zeta potential was measured using the Zeta PALS instrument from Brookhaven. Agarose gel electrophoresis was used to verify whether Apt was linked to Au NRs. UV–vis absorption spectroscopy was performed using the S-3100 photodiode array to obtain UV–vis

spectra (Scinco Co., South Korea). FT-IR spectra were obtained using the FT-IR spectrometer (IRPrestige-21, Japanese Shimadzu). DOX/Au-Apt@ZIF-8 was subjected to XRD (Nippon Science-SmartLab), EDS, and mapping of the energy spectrum (OXFORD Ultim Max 65). The DOX/Au-Apt@ZIF-8 solution was subjected to 808 nm NIR irradiation for 6 min with different powers and concentrations, and the temperature was recorded every 30 s. The temperature and time curves at different powers and concentrations were then plotted. Similarly, to evaluate the photothermal conversion efficiency, 400 μg/mL DOX/Au-Apt@ZIF-8 solution was subjected to 808 nm NIR irradiation (2 W/cm<sup>2</sup>) for 3 min. Then, the laser was turned off for 3 min, and the temperature was recorded for four cycles to draw the temperature and time curves. In the same manner, the 400 μg/mL DOX/Au-Apt@ZIF-8 solution was subjected to 808 nm NIR irradiation (2 W/cm<sup>2</sup>) until the temperature did not change. Then, the laser was turned off, and the solution temperature was lowered to room temperature. Temperature changes were recorded and a cooling curve was drawn. Thermal images of the DOX/Au-Apt@ZIF-8 solution at different concentrations were captured using the infrared camera at different time points (1, 2, 3, 4, and 5 min) with an accuracy of 0.1 °C. The formula for calculating the photothermal conversion efficiency is given below<sup>41</sup>

$$\tau_s = \frac{mC_p}{hS} \quad (1)$$

$$\eta = \frac{hS(T_{\max} - T_{\text{surr}}) - Q_s}{I(1 - 10A^4)} \quad (2)$$

$\tau_s$ : system heat transfer time constant (s);  $m$ : the mass of ultrapure water (g);  $C_p$ : specific heat capacity of ultrapure water (J/(g·°C));  $h$ : heat transfer coefficient [mW/(m<sup>2</sup>·°C)];  $S$ : area of quartz cuvette (m<sup>2</sup>);  $\eta$ : heat transfer efficiency;  $T_{\max}$ : the maximum temperature that the system can reach (°C);  $T_{\text{surr}}$ : the initial temperature of the system (°C);  $Q_s$ : adapting to the initial baseline energy input of colorimetric dishes and ultrapure water (J);  $I$ : the power size of the 808 laser transmitter (mW/cm<sup>2</sup>);  $A^4$ : the UV absorbance of the sample at 808 nm.

**Detection of Drug Loading and Release Rates of DOX/Au-Apt@ZIF-8.** First, 2 mg of DOX/Au-Apt@ZIF-8 was dissolved in 4 mL of phosphate-buffered saline (PBS) having different pH values (1.2, 4.5, 6.8, and 7.4). Then, the solution was sealed in a dialysis bag (2000 kDa). Subsequently, the dialysis bag containing DOX/Au-Apt@ZIF-8 solution was placed into a small beaker containing 40 mL of PBS at different pHs (1.2, 4.5, 6.8, and 7.4), and the beaker was placed in a shaker at 37 °C to avoid light. Using DOX as a model drug release, the absorbance was measured at 482 nm by using an ultraviolet spectrophotometer with intervals of sampling. The solution volume in the beaker was maintained by supplementing it with additional liquid. The drug loading and release rates were determined by combining Formulas 1 and 2.<sup>42</sup>

$$m = \frac{a}{b} \quad (a)$$

$$M = \frac{A}{B} \quad (b)$$

where  $m$  is the load rate;  $a$  is the weight of the drug contained in the material;  $b$  is the amount of drug input during the synthesis reaction;  $M$  is the drug release rate;  $A$  is the content of the drug in PBS;  $B$  is the content of the drug loaded in the material.

**Cell Culture.** MCF-7 cells were cultured with DMEM (containing 10% fetal bovine serum and 1% penicillin and streptomycin) in an incubator at 37 °C and under 5% CO<sub>2</sub>.<sup>43</sup>

**In Vitro Cell Uptake and Fluorescent Imaging.** The MCF-7 cells were seeded into 6-well plates (1 × 10<sup>6</sup> cells/well) for 24 h. Then, the cells were incubated with DOX (10 μg/mL) and DOX/Au-Apt@ZIF-8 (based on the DOX content and concentration of 10 μg/mL) for 2 and 6 h, respectively. The cells were fixed by incubating with 4% paraformaldehyde for 10 min and then washed with PBS.



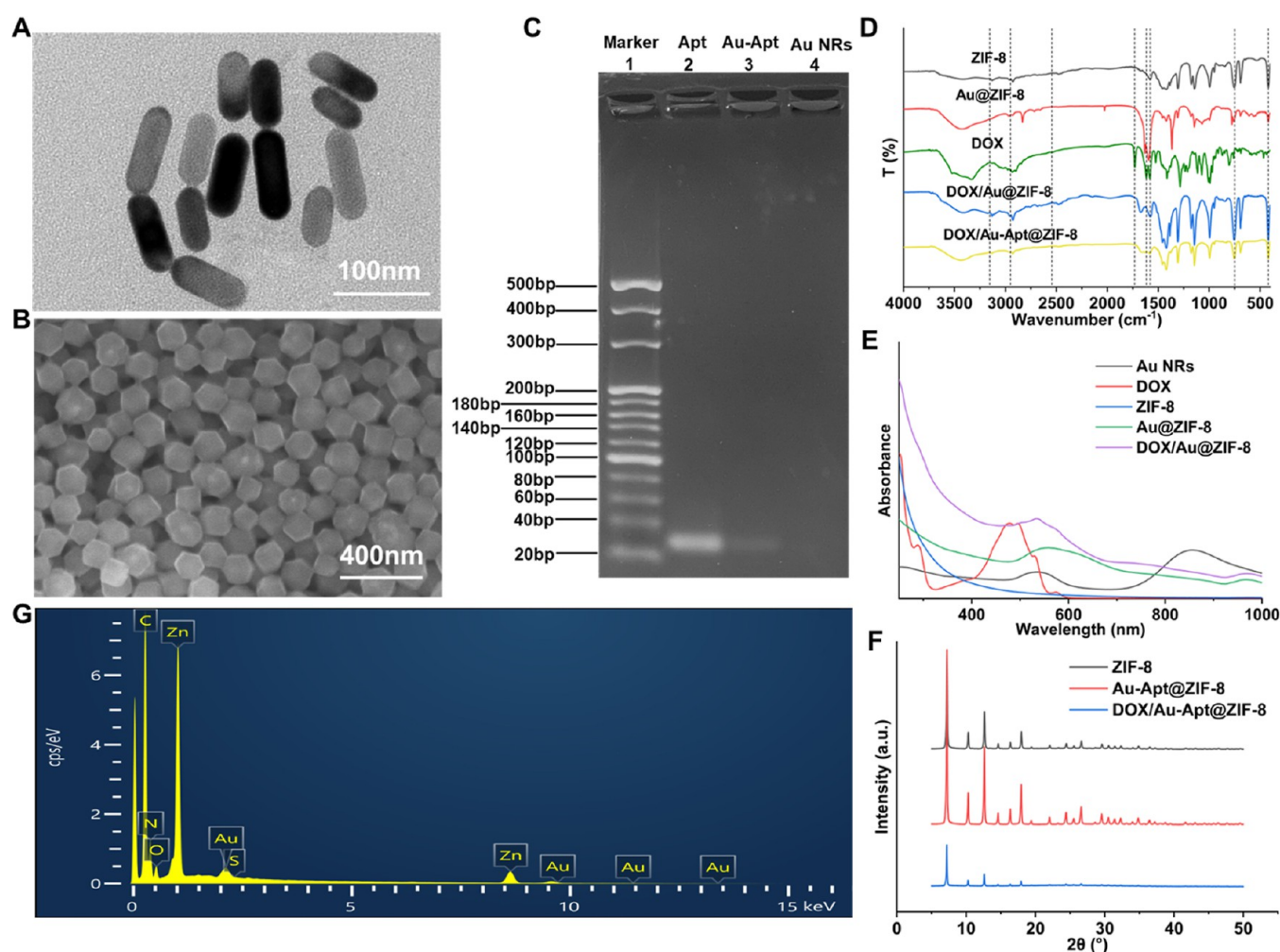


**Figure 1.** Synthesis and characterization of DOX/Au-Apt@ZIF-8. (A) TEM images of Au NRs. (B) SEM images of DOX/Au-Apt@ZIF-8. (C) Agarose gel electrophoresis of free Apt, Au-Apt, and Au NRs. (D) Fourier-transformed infrared spectra of ZIF-8, Au@ZIF-8, DOX, DOX/Au@ZIF-8, and DOX/Au-Apt@ZIF-8. (E) UV absorption spectra of Au NRs, DOX, ZIF-8, Au@ZIF-8, and DOX/Au@ZIF-8. (F) XRD of ZIF-8, Au@ZIF-8, and DOX/Au-Apt@ZIF-8. (G) EDS spectra of DOX/Au-Apt@ZIF-8.

Then, 500  $\mu\text{L}$  of 4',6-diamidino-2-phenylindole was added to the cells with light avoidance for 15 min, and the cells were washed again with PBS. Finally, the cells were overlaid on a microscope slide. The observation area and layer were determined under a fluorescence microscope, and the fluorescence images were collected.

**Detection of the Cell Cycle.** The MCF-7 cells were seeded into 24-well plates ( $1 \times 10^5$  cells/well) for 24 h. The drug groups studied were DOX, DOX/Au-Apt@ZIF-8, and DOX/Au-Apt@ZIF-8 + NIR (based on the DOX content and concentration of 5  $\mu\text{g}/\text{mL}$ ). The cells were incubated with the respective drugs for 24 h. The cells in the DOX/Au-Apt@ZIF-8 + NIR group were subjected to 808 nm NIR irradiation ( $1.5 \text{ W}/\text{cm}^2$ ) for 5 min. Then, all the cells were collected and washed with precooled PBS, fixed at 4  $^\circ\text{C}$  through treatment with precooled 70% ethanol for 24 h, and washed twice with PBS. RNase (100  $\mu\text{L}$ , 1 mg/mL) was then added to the suspended cells. The cells were then bathed in a 37  $^\circ\text{C}$  warm bath away from light for 30 min. The propidium iodide (PI) dyeing solution (400  $\mu\text{L}$ , 50  $\mu\text{g}/\text{mL}$ ) was added to the cells at 4  $^\circ\text{C}$  with light avoidance for 15 min, and the data were obtained using FlowJo software.

**Detection of Cytotoxicity.** The CCK-8 method was used to evaluate cell viability before and after drug treatment. Logarithmically grown MCF-7 cells were seeded into 96-well plates ( $1 \times 10^4$  cells/well) for 24 h. No treatment was used as a control. In the drug groups, the cells were incubated with diverse concentrations (0, 0.625, 1.25, 2.5, 5, 10, and 20  $\mu\text{g}/\text{mL}$ ) of DOX, Au-Apt@ZIF-8, DOX/Au@ZIF-

8, DOX-Apt@ZIF-8, DOX/Au-Apt@ZIF-8, DOX-Apt@ZIF-8 + NIR, Au-Apt@ZIF-8 + NIR, or DOX/Au-Apt@ZIF-8 + NIR (based on the DOX content and concentration) solutions for 24 h. The cells in the Au-Apt@ZIF-8 + NIR and DOX/Au-Apt@ZIF-8 + NIR groups were subjected to 808 nm NIR irradiation ( $1.5 \text{ W}/\text{cm}^2$ ) for 5 min. The CCK-8 reagent and the medium were added to the well at a 1:10 ratio for coincubation away from the light at 37  $^\circ\text{C}$  for 1 h. The absorbance was measured at 450 nm to calculate the cell survival rate.

**Detection of Apoptosis.** The MCF-7 cells were seeded into 6-well plates ( $1 \times 10^6$  cells/well) for 24 h. The drug administration groups were DOX, DOX/Au-Apt@ZIF-8, and DOX/Au-Apt@ZIF-8 + NIR (based on the DOX content and concentration). The cells were incubated with different concentrations (2.5, 5, and 10  $\mu\text{g}/\text{mL}$ ) of the drug for 24 h. The cells in the DOX/Au-Apt@ZIF-8 + NIR group were subjected to 808 nm NIR irradiation ( $1.5 \text{ W}/\text{cm}^2$ ) for 5 min. The cells were collected and washed with precooled PBS. After the cells were resuspended with 500  $\mu\text{L}$  of the binding buffer, the cells were treated with 5  $\mu\text{L}$  of Annexin V-FITC and 5  $\mu\text{L}$  of PI for 5–15 min under dark conditions. Cell apoptosis was observed through flow cytometry.

**Study on Antitumor Activity in Vivo.** The BALB/c female nude mice were bought from Nanjing Qing Long Shan Animal Farm and raised under a specific pathogen-free condition. The MCF-7 cells ( $5 \times 10^6$  cells/100  $\mu\text{L}$ ) were injected into the shoulder of the nude mice. After tumor growth for 5 days, the mice were randomly assigned to four groups (PBS, DOX, DOX/Au-Apt@ZIF-8, and DOX/Au Apt@

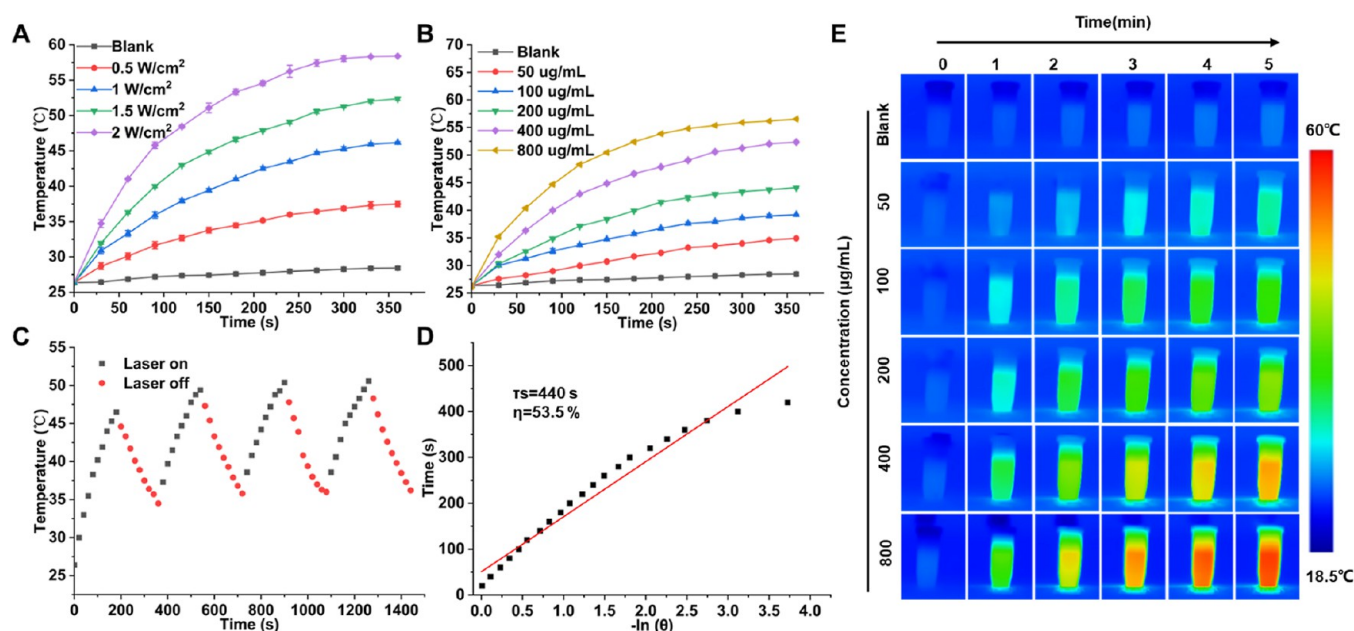


**Figure 2.** Photothermal effect of DOX/Au-Apt@ZIF-8. (A) Photothermal temperature rise curves of 808 nm NIR-treated DOX/Au-Apt@ZIF-8 (400 μg/mL) at different irradiation intensities (0.5, 1.0, 1.5, and 2.0 W/cm²). (B) Photothermal temperature rise curves of DOX/Au-Apt@ZIF-8 (50, 100, 200, 400, and 800 μg/mL) at different concentrations were subjected to 808 nm NIR irradiation (2 W/cm²). (C) Photothermal stability curve of DOX/Au-Apt@ZIF-8. (D) Linear regression curves of time to  $-\ln \theta$  for DOX/Au-Apt@ZIF-8 (400 μg/mL). (E) Thermal images of DOX/Au-Apt@ZIF-8 (50, 100, 200, 400, and 800 μg/mL) at different concentrations subjected to 808 nm NIR irradiation.

ZIF-8 + NIR). The tumor site was exposed to 808 nm NIR (1.5 W/cm²) for 5 min in the irradiation group after drug treatment for 24 h. On the 14th day of treatment, an *in vivo* photothermal imaging test was conducted on the mice in the PBS, DOX, and DOX/Au-Apt@ZIF-8 groups. Finally, the mice were euthanized using the cervical dislocation method. The main organs and tumor tissues of the mice were collected for HE and TUNEL staining. The tumor tissues were weighed, and the tumor volume was calculated [ $V = \pi(a \times b^2)/6$ ]. This study was approved by the Animal Experimental Ethics Committee of Wannan Medical College (approval number: LLSC-2022-018; date of approval: March 4, 2022).

**In Vivo Safety Evaluation of Au-Apt@ZIF-8.** To evaluate the *in vivo* safety of Au-Apt@ZIF-8 nanocarriers, normal mice were randomly divided into four groups (PBS, NIR, Au@ZIF-8, and Au@ZIF-8 + NIR). Each group of mice was injected with the drugs at a fixed time every day for 14 consecutive days. The mice were weighed every alternate day. After the treatment, the major organs of the mice were collected and stained with hematoxylin and eosin (HE).

**Statistical Analysis.** Statistical analysis was performed by SPSS Statistics 29.0.1.0. Statistical analysis was conducted by the *t*-test for comparisons between two groups and by one-way ANOVA for comparisons of more than three groups. Data are presented as mean  $\pm$  SD ( $n = 3-5$ ). \* $P < 0.05$ , \*\* $P < 0.01$ , \*\*\* $P < 0.001$ , difference with the control group.

## RESULTS AND DISCUSSION

**Characterization of DOX/Au-Apt@ZIF-8.** The TEM analysis revealed that Au NRs were a short rod with uniform morphology (Figure 1A). The SEM analysis revealed that DOX/Au-Apt@ZIF-8 has a uniform size, morphology, and good dispersion (Figure 1B). DLS (Figure S1A) analysis revealed that the average particle sizes of Au NRs and Au@ZIF-8 were approximately 68 and 158 nm, respectively. The average particle size of the modified DOX/Au-Apt@ZIF-8 was approximately 168 nm, which is consistent with the SEM observation. The results thus indicate that ZIF-8 encapsulated

DOX and Apt-modified Au NRs, thereby increasing their particle size.

Agarose gel electrophoresis (Figure 1C) revealed that free Apt moved downward in the gel (lane 2). However, only part of Au-Apt was not linked to Au NRs and moved downward in the gel (lane 3). Nanoparticles without Apt modifications generated no signals (lane 4). The experimental results revealed that at least some Apt was coupled with Au NRs.

The FT-IR spectra clearly exhibited the characteristic absorption peaks of ZIF-8 at 3135, 2926, 1579, 1421, 1307, 1175, 1142, 995, 756, 680, and 420 cm<sup>-1</sup> (Figure 1D), which is consistent with the results of previous studies.<sup>44</sup> The peaks at 3135 and 2926 cm<sup>-1</sup> are attributed to the aromatic and aliphatic C–H contraction of imidazole groups; the peaks in the 1350–1500 cm<sup>-1</sup> band are derived from the stretching of imidazole rings; the peaks at 995 and 1142 cm<sup>-1</sup> are attributed to the stretching of the aromatic group; the 900–1350 cm<sup>-1</sup> band and the band <850 cm<sup>-1</sup> are associated with in-plane and out-of-plane bending of the imidazole ring, respectively. The peaks at 1579 and 420 cm<sup>-1</sup> are axial deformations of C=N and Zn–N, respectively.<sup>45,46</sup> When compared with ZIF-8, the characteristic peaks of Au@ZIF-8 exhibited no change, indicating that Au NR loading caused no damage to the structure of ZIF-8. Compared with Au@ZIF-8, DOX/Au@ZIF-8 had a C–C ring tension stretching vibration peak at 1675 cm<sup>-1</sup>, a C=O stretching vibration peak at 1576 cm<sup>-1</sup>, a C–H bond bending vibration peak at 1414 cm<sup>-1</sup>, a C=N stretching vibration peak at 1309 cm<sup>-1</sup>, a C–O–C tensile vibration peak at 1153 cm<sup>-1</sup>, and a N–H tensile vibration peak at 993 cm<sup>-1</sup>, indicating that DOX was loaded to Au@ZIF-8. The characteristic peak at 2526 cm<sup>-1</sup> in FT-IR was observed due to S–H stretching. The disappearance of this peak indicated Au–S bond formation,<sup>47</sup> whereas the S–H peak did not appear in the infrared spectrum of DOX/Au-Apt@ZIF-8. These results thus indicate that Apt was linked to Au NRs.



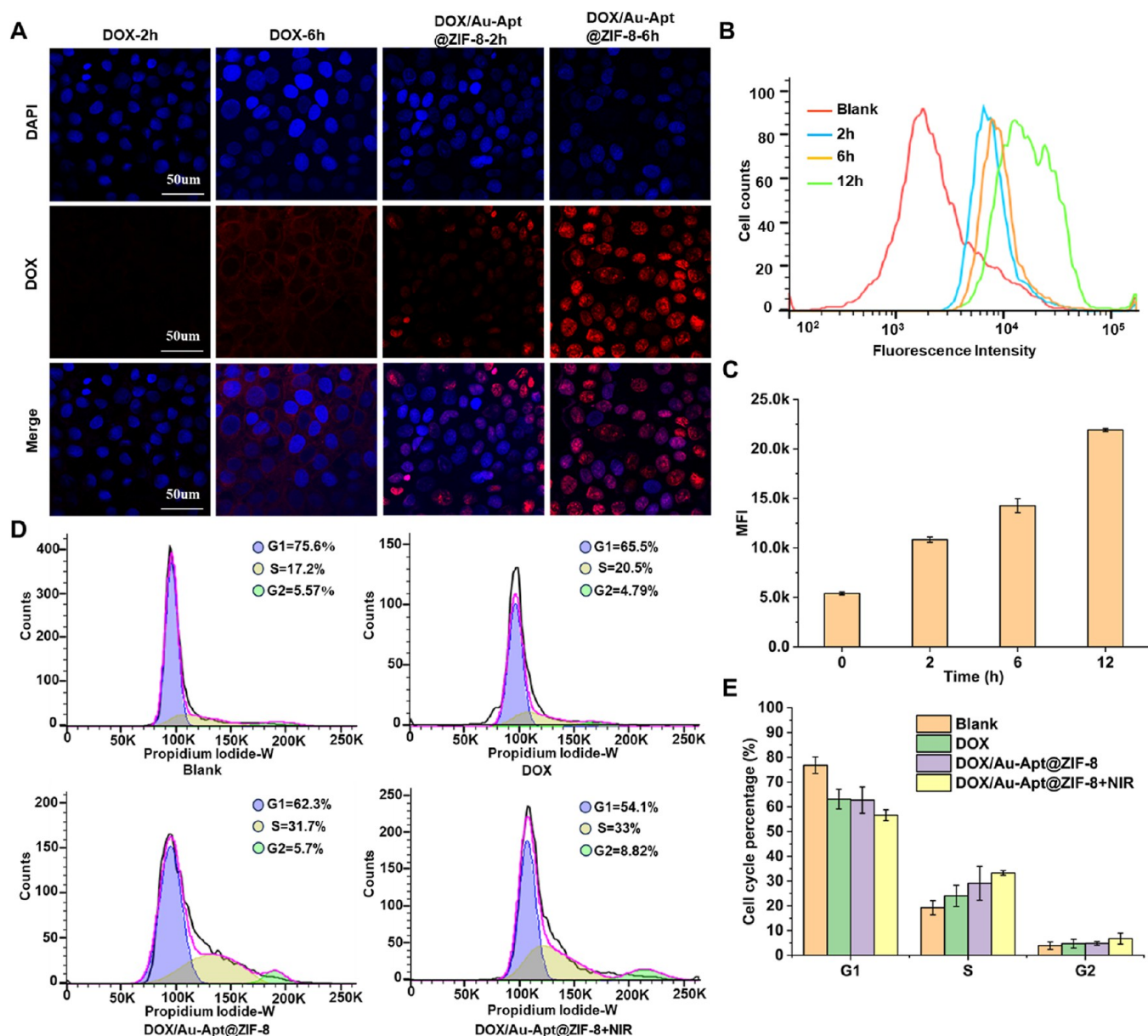


**Figure 3.** (A) Confocal laser microscopy images of DOX and DOX/Au-Apt@ZIF-8. (B,C) Average fluorescence intensity of DOX/Au-Apt@ZIF-8 cell uptake at different treatment times (0, 2, 6, and 12 h). (D,E) Cell cycle analysis of MCF-7 cells treated with DOX, DOX/Au-Apt@ZIF-8, and DOX/Au-Apt@ZIF-8 + NIR.

Past literature has shown that the electrons of Au NRs oscillated at different frequencies on the transverse and longitudinal surfaces, thereby exhibiting 2 different resonance frequencies, resulting in transmission surface plasmon resonance (TSPR) and localized surface plasmon resonance (LSPR).<sup>48</sup> The vis–NIR spectrum revealed double peaks of Au NRs at 534 and 855 nm, which is consistent with the spectrum characteristics of Au NRs (Figure 1E). The experimental results showed that the vis–NIR of Au@ZIF-8 was 557 and 972 nm after wrapping Au NRs with ZIF-8, indicating that the wrapping of ZIF-8 affects the absorption peak of Au NRs. When compared to the UV absorption peak of DOX, the UV absorption of DOX/Au@ZIF-8 was red-shifted, and the absorption peak of Au@ZIF-8 shifted from 557 to 536 nm, which is consistent with the literature findings.<sup>49</sup>

Through the zeta potential analysis, we found that Au NRs had a positive charge and a zeta potential of approximately

15.5 mV (Figure S1B). Because Au-Apt is coated with ZIF-8 by the in situ growth method, the potential of Au-Apt@ZIF-8 synthesized with ZIF-8 as the frame increases to approximately 17.4 mV. The DOX molecule becomes positively charged upon dehydrochlorination;<sup>50</sup> therefore, the potential of DOX/Au-Apt@ZIF-8 further increases to approximately 22.2 mV after loading DOX.

The XRD values of ZIF-8, Au-Apt@ZIF-8, and DOX/Au-Apt@ZIF-8 were  $2\theta = 7.4, 10.4, 12.8, 14.7, 16.5,$  and  $18.1^\circ$ , respectively (Figure 1F).<sup>51</sup> The main peaks of Au-Apt@ZIF-8 and DOX/Au-Apt@ZIF-8 were consistent. This indicated that the introduction of Au-Apt and DOX caused no damage to the ZIF shell,<sup>52,53</sup> which is consistent with the SEM results.

In addition, EDS (Figure 1G) and mapping of the energy spectrum (Figure S1C) unveiled that DOX/Au-Apt@ZIF-8 nanocomposites were directly composed of C, N, O, Zn, Au, and S elements.

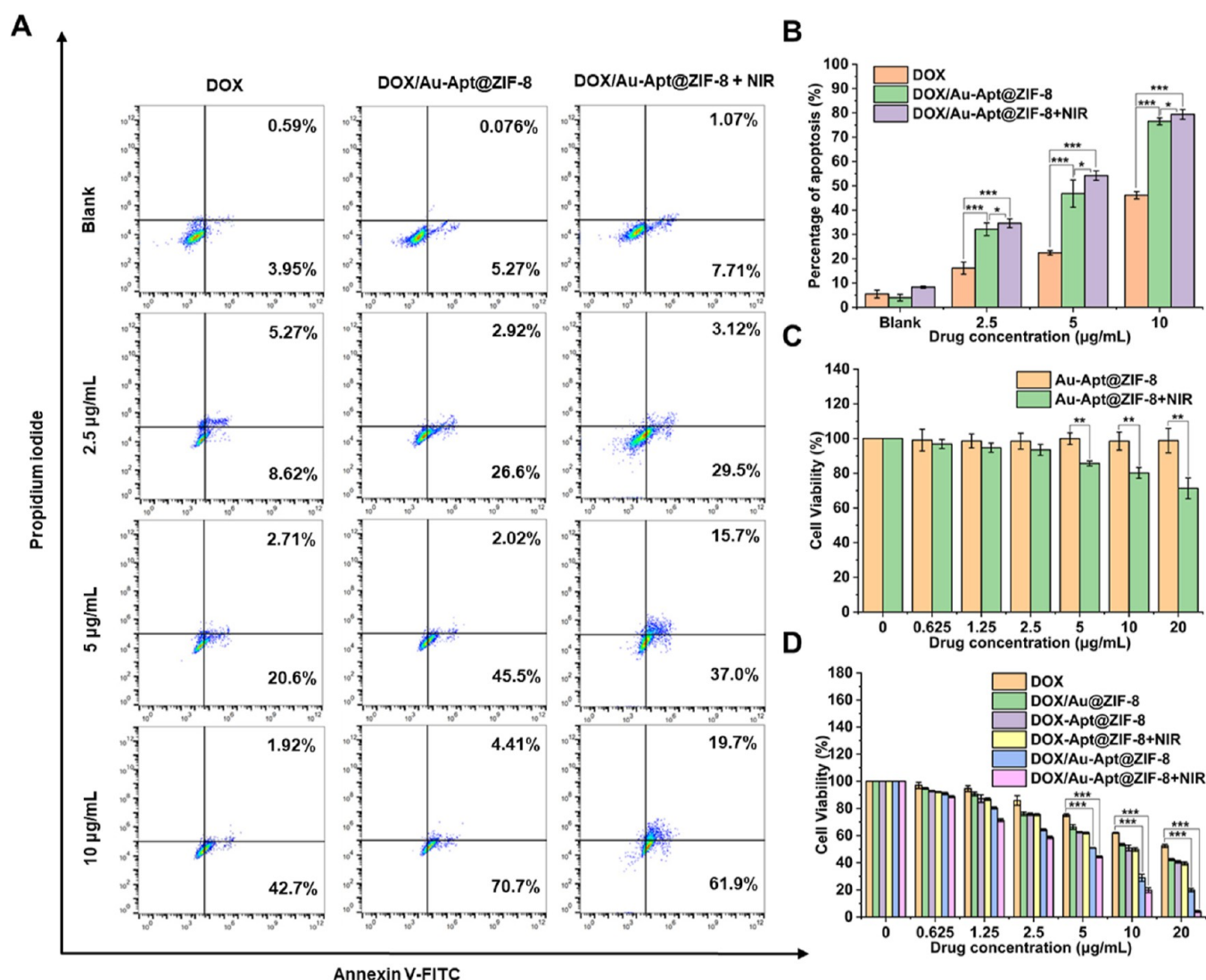


**Figure 4.** (A,B) Flow cytometry analysis of MCF-7 cells apoptosis induced by DOX, DOX/Au-Apt@ZIF-8, and DOX/Au-Apt@ZIF-8 + NIR. (C) Cell survival rate after coculture of Au-Apt@ZIF-8 and Au-Apt@ZIF-8 + NIR with MCF-7 cells at different concentrations. (D) Cell survival rate of MCF-7 cells treated with different concentrations of DOX, DOX/Au@ZIF-8, DOX-Apt@ZIF-8, DOX-Apt@ZIF-8 + NIR, DOX/Au-Apt@ZIF-8, and DOX/Au-Apt@ZIF-8 + NIR. Data are presented as mean  $\pm$  SD ( $n = 3-5$ ). \* $P < 0.05$ , \*\* $P < 0.01$ , \*\*\* $P < 0.001$ , difference with the control group.

Based on these results, we believe that DOX/Au-Apt@ZIF-8 was successfully synthesized.

**In Vitro Photothermal Efficiency.** Au NRs subjected to 808 nm NIR irradiation can convert light energy to heat energy.<sup>54</sup> To verify whether ZIF-8 can produce a photothermal effect after Au NRs were loaded, 400  $\mu\text{g/mL}$  DOX/Au-Apt@ZIF-8 solution was subjected to NIR irradiation of different intensities for 6 min (Figure 2A). The solution temperature increased with increasing irradiation time. When the irradiation intensity was 1.5  $\text{W/cm}^2$ , the temperature increased to  $>40^\circ\text{C}$ , which led to the induction of cell apoptosis.<sup>55,56</sup> The temperature increase with different concentrations was found to be concentration-dependent when the irradiation intensity was 2  $\text{W/cm}^2$  (Figure 2B,E). When the concentration of DOX/Au-Apt@ZIF-8 was  $>400 \mu\text{g/mL}$ , the temperature reached  $>50^\circ\text{C}$ , showing good thermal imaging capability. According to these results, the Au NR-loaded nanoparticle drug carrier system possessed good photothermal properties. To determine the photothermal stability of DOX/Au-Apt@

ZIF-8, the activator was turned off after 3 min of NIR irradiation and turned on again after 3 min of cooling; this cycle was repeated 4 times. According to the analysis shown in Figure 2C, each time, the temperature of DOX/Au-Apt@ZIF-8 after 3 min of NIR irradiation was higher than that of the previous time, and the maximum temperature was maintained at approximately  $50^\circ\text{C}$ . This observation indicated that DOX/Au-Apt@ZIF-8 developed good photothermal stability in a short span. Based on Formulas 1 and 2, when the DOX/Au-Apt@ZIF-8 solution with a 400  $\mu\text{g/mL}$  concentration was subjected to 808 nm NIR irradiation, its  $\Delta T_{\text{max}}$  was  $24.9^\circ\text{C}$  and  $\tau_s$  was 440 s, while the thermal conversion efficiency reached 53.5% (Figures 2D and S2). These results proved that DOX/Au-Apt@ZIF-8 had excellent photothermal heating performance, photothermal imaging ability, photothermal stability, and photothermal conversion effect. Therefore, a relatively mild irradiation intensity (1.5  $\text{W/cm}^2$ , 5 min) was selected as the photothermal conditions for subsequent cell

experiments and animal experiments, so as to avoid excessive temperature-induced damage to other normal tissues.

**Analysis of Drug Loading and Release Rates.** The UV absorption values measured of the supernatant retained by synthesized DOX/Au-Apt@ZIF-8 nanoparticles at different ratios (1:2, 1:1, and 2:1) were brought into the standard curve (Figure S3A), after which, the DOX drug loading rate was calculated according to a and b. This DOX drug loading rate was approximately 24.69, 34.56, and 29%, respectively. The nanoparticles synthesized in a 1:1 ratio was selected for the experimental study based on the drug loading rate achieved through different proportions.

As the coordination bond in ZIF-8 is sensitive to acidic environments, it undergoes acid-responsive cleavage and releases chemotherapeutic drugs.<sup>10</sup> Hence, we evaluated the cumulative release of DOX/Au-Apt@ZIF-8 in artificially simulated blood (pH = 7.4), artificially simulated intestinal fluid (pH = 6.5), artificially simulated tumor environment (pH = 4.5), and artificially simulated gastric fluid (pH = 1.2). The cumulative drug release rates were 10.17, 14.02, 31.11, and 37.51%, respectively, at different pHs (7.4, 6.5, 4.5, and 1.2) after 24 h of incubation, and those after 48 h of incubation tended to be stable with cumulative drug release rates of approximately 10.34, 15.86, 54.58, and 60.44%, respectively (Figure S3B). The experimental results revealed that drug release increased with decreasing pH value, indicating that DOX/Au-Apt@ZIF-8 could effectively release DOX in the acidic environment of the tumor cells. When the treatment time reached 96 h, the cumulative DOX release remained at a certain level, indicating that the DOX/Au-Apt@ZIF-8 carrier material was conducive to a slow drug release.

**Cell Uptake and Cell Cycle Analysis.** To determine whether DOX/Au-Apt@ZIF-8 targets tumors, a cell uptake assay was performed to conduct localization experiments on DOX. On comparing the fluorescence images of MCF-7 cell-ingested DOX and DOX/Au-Apt@ZIF-8 (Figure 3A), we observed red fluorescence in the cells after 2 h of treatment, which confirmed that DOX was ingested by MCF-7. Moreover, the red fluorescence intensity was markedly higher in the DOX/Au-Apt@ZIF-8 group than in the DOX-alone treatment group under the same treatment time. The red fluorescence was primarily concentrated in the nucleus and its surrounding region. When the treatment time was 6 h, the fluorescence intensity was more evident, indicating that DOX/Au-Apt@ZIF-8 transported DOX into cells more efficiently, and thus showed a good ability to target tumor cells. In addition, the average fluorescence intensity of MCF-7 cells incubated with DOX/Au-Apt@ZIF-8 for different times (0, 2, 6, and 12 h) was detected through flow cytometry. The average fluorescence intensity of cells increased in a time-dependent manner as the action time was extended (Figure 3B,C), which suggested that MCF-7 cells had a good capacity to uptake DOX/Au-Apt@ZIF-8.

DOX is a nonspecific cell cycle-blocking drug that inhibits DNA replication and topoisomerase activity, which breaks protein-linked double-stranded and single-stranded DNA, ultimately leading to cytotoxic DNA damage and cell death.<sup>57–59</sup> In addition, laser irradiation with nanomaterials having photothermal properties has a certain effect on the cell cycle arrest.<sup>60</sup> We then verified whether DOX/Au-Apt@ZIF-8 nanoparticles can further improve the cell cycle blocking effect of DOX on MCF-7 cells. The cells were treated with 5  $\mu\text{g/mL}$  DOX and DOX/Au-Apt@ZIF-8 for 24 h and subjected to NIR

irradiation for 5 min. When compared with the blank group, the G1 phase decreased and the S phase increased in the DOX and DOX/Au-Apt@ZIF-8 groups (Figure 3D,E). This observation indicated that the MCF-7 cells were blocked in the S phase in the drug group; this blocking effect was more significant in the DOX/Au-Apt@ZIF-8 group than in the DOX group. This finding confirmed that the S phase arrest is one of the mechanisms through which DOX/Au-Apt@ZIF-8 inhibits cell proliferation. Moreover, the proportion of the S phase increased by 4.17% in the DOX/Au-Apt@ZIF-8 + NIR group than in the DOX/Au-Apt@ZIF-8 group. We thus speculated that PTT induces cell sensitivity to targeted nanomaterials by interfering with the cell cycle, thereby improving the therapeutic effect against breast cancer.

**Cell Apoptosis and Cytotoxicity Analysis.** Drug carriers are constructed for the better delivery of antitumor drugs so as to allow them to exert their complete antitumor effect. Therefore, we conducted apoptosis and cytotoxicity analyses to detect whether DOX/Au-Apt@ZIF-8 has better antitumor effects and to determine the toxicity of the material itself. The apoptosis rate in the different treatment groups increased in a drug concentration-dependent manner (Figure 4A,B). At the same concentration, the apoptosis rate of the DOX group was significantly lower than that of the other treatment groups, whereas the apoptosis rate of the DOX/Au-Apt@ZIF-8 + NIR group was higher than that of the DOX/Au-Apt@ZIF-8 group. At the concentration of 10  $\mu\text{g/mL}$ , the apoptosis rates of the MCF-7 cells were 44.62, 75.11, and 81.60% in the DOX, DOX-Apt@ZIF-8, and DOX/Au-Apt@ZIF-8 + NIR groups, respectively. This finding suggests that the DOX/Au-Apt@ZIF-8 nanoparticle drug delivery system induced apoptosis more effectively, which is possibly attributable to the good targeting ability of DOX/Au-Apt@ZIF-8 that enables DOX to enrich tumor cells. Moreover, photothermal irradiation further improved the apoptosis-inducing ability of the drug delivery system and exhibited a stronger antitumor effect.

Based on the MCF-7 cell survival rate result, we concluded that the carrier material was slightly cytotoxic to MCF-7 cells (Figure 4C). The NIR irradiated group exhibited a concentration-dependent decline in the cell survival rate as the concentration of the unloaded drug Au-Apt@ZIF-8 increased, indicating that, with the increase of Au-Apt@ZIF-8 concentration, the number of Au NRs ingested by cells also increased, and, with the improvement of the photothermal effect, the antitumor effect of gold nanorods became stronger. Furthermore, we compared the effects of DOX, DOX/Au@ZIF-8, DOX/-Apt@ZIF-8, DOX/-Apt@ZIF-8 + NIR, DOX/Au-Apt@ZIF-8, and DOX/Au-Apt@ZIF-8 + NIR on the MCF-7 cell survival rate. All drug treatment groups exerted a certain inhibitory effect on survival (Figure 4D), and as the drug concentration increased, the cell survival rate decreased in a concentration-dependent manner. Among them, the DOX/Au-Apt@ZIF-8 group and the DOX/Au-Apt@ZIF-8 + NIR group had a particularly obvious inhibitory effect on the cell survival rate. At 5  $\mu\text{g/mL}$ , the cell survival rate was approximately 51.06 and 44.32%, respectively. These results indicated that drug delivery systems involving Apt have a higher inhibitory effect on tumor growth, which may be related to their ability to target tumor cells and promote more drug aggregation in these cells. However, NIR irradiation further improved the ability of DOX/Au-Apt@ZIF-8 to inhibit tumor growth, indicating that, as the drug concentration increased, Au NRs with a photothermal effect accumulated in the cells,



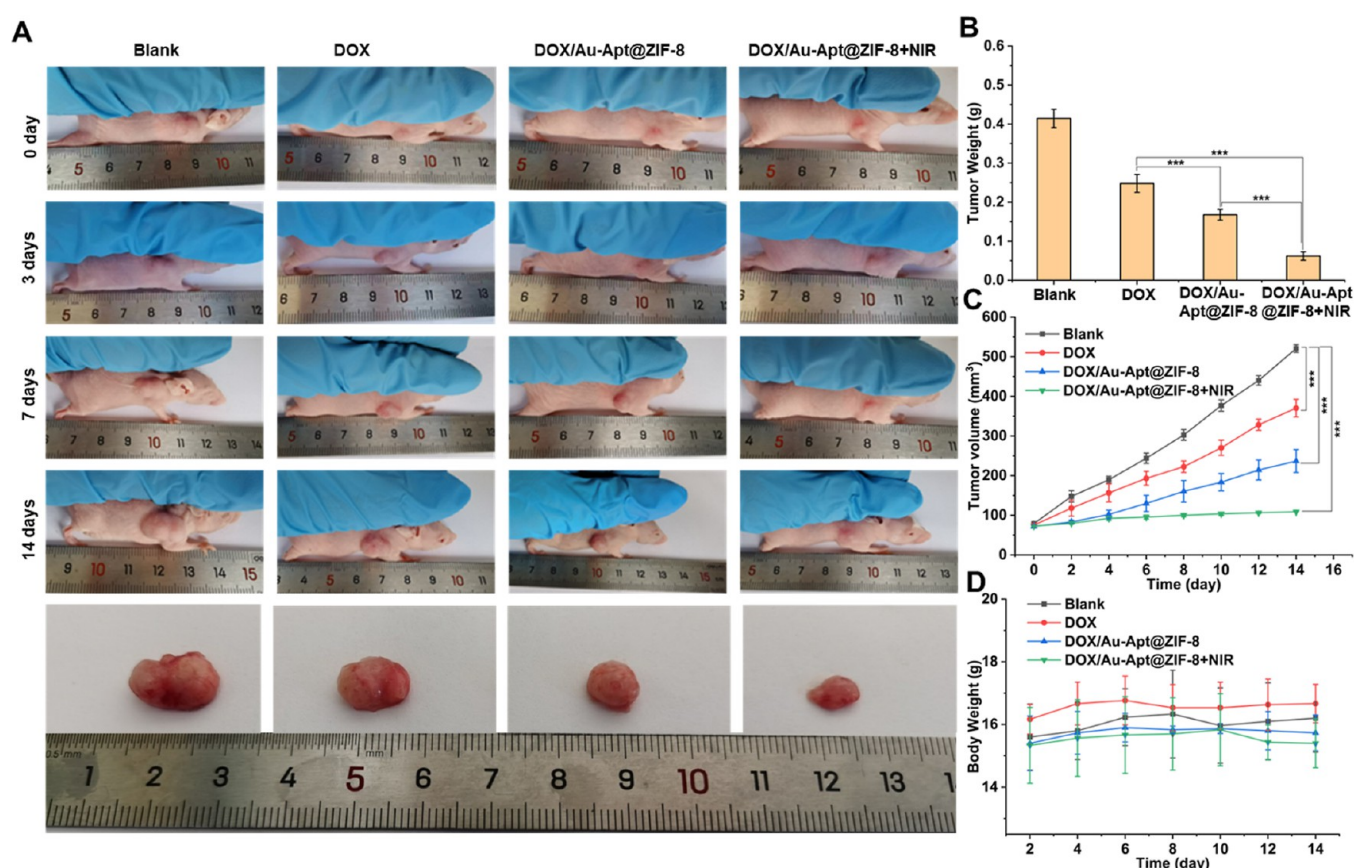


**Figure 5.** Effects of DOX, DOX/Au-Apt@ZIF-8, and DOX/Au-Apt@ZIF-8 + NIR on nude mice with breast cancer. (A) Changes in tumor diameter. (B) Relative tumor mass. (C) Changes in tumor volume. (D) Changes in the body weight of the mice. Data are presented as mean  $\pm$  SD ( $n = 3-5$ ). \*\*\* $P < 0.001$ , difference with the control group.

thereby enhancing the photothermal effect of inhibiting tumor cell survival. Therefore, when compared with the other three treatment groups, the DOX/Au-Apt@ZIF-8 + NIR group exerted the best inhibitory effect on tumor cell survival, indicating that the multimodal combination of chemotherapy–target–PTT can exert the best effect when compared with chemotherapy alone.

**In Vivo Anticancer Effects of DOX/Au-Apt@ZIF-8.** To further assess the antitumor activity of DOX/Au-Apt@ZIF-8, a nude mice model of a breast cancer-bearing tumor was established, and changes in the tumor size with treatment were recorded in the mice (Figure 5A). When compared with the blank group, tumor diameter decreased to varying degrees in the DOX, DOX/Au-Apt@ZIF-8, and DOX/Au-Apt@ZIF-8 + NIR groups as the treatment time increased. Among these three treatments, DOX/Au-Apt@ZIF-8 + NIR exhibited the strongest inhibitory effect on tumor growth. On the 14th day of treatment, the tumor diameter in the control group was 1.35 cm, whereas that in the DOX/Au-Apt@ZIF-8 + NIR group was only 0.7 cm. The tumor weight (Figure 5B) and volume (Figure 5C) of mice in the different treatment groups also complied with the aforementioned findings. The tumor weight and volume in the DOX/Au-Apt@ZIF-8 + NIR group were the smallest at approximately 0.062 g and 108.87 mm<sup>3</sup>, respectively. This finding indicated that the drug treatments had an inhibitory effect on tumor growth, with DOX/Au-Apt@ZIF-8 + NIR exerting the strongest effect. Based on the data of the DOX and DOX/Au-Apt@ZIF-8 groups, we can infer that this inhibitory effect is mostly due to the action of DOX. The

tumor growth rate was significantly lower in the DOX/Au-Apt@ZIF-8 group than in the DOX group. While DOX/Au-Apt@ZIF-8 delivers DOX, Au NRs can be delivered to tumor cells at the same time. Tumor cells are subjected to the dual action of chemotherapeutic drugs and PTT. Therefore, tumor cells exhibited the slowest growth rate and experienced the strongest antitumor effect in the DOX/Au-Apt@ZIF-8 + NIR group. Furthermore, the weight of the mice exhibited no significant fluctuations (Figure 5D), indicating that DOX/Au-Apt@ZIF-8 was tolerated in the mice and showed no acute side effects.

**In Vivo Thermal Imaging and Effects of DOX/Au-Apt@ZIF-8 on Tumor Apoptosis.** To further verify whether DOX/Au-Apt@ZIF-8 exhibits good photothermal effects *in vivo*, photothermal imaging analysis was performed in the mice (Figure 6A). The results revealed that, after 5 min of 808 nm NIR irradiation, the temperature of the tumor site in the DOX/Au-Apt@ZIF-8 + NIR group increased rapidly, and the maximum temperature reached was 42.3 °C, whereas it remained unchanged in the other two groups. The effective drug carriers targeted the Au NRs and converged on the tumor site, which induced the photothermal reaction.

To determine whether the DOX/Au-Apt@ZIF-8 delivery system can effectively induce tumor cell apoptosis, the effect of this system on tumor cell apoptosis was investigated through TUNEL staining (Figure 6B). When compared with the blank group, the number of apoptotic cells increased significantly in the other three groups. Among these three groups, the number of apoptotic cells was the highest in the DOX/Au-Apt@ZIF-8

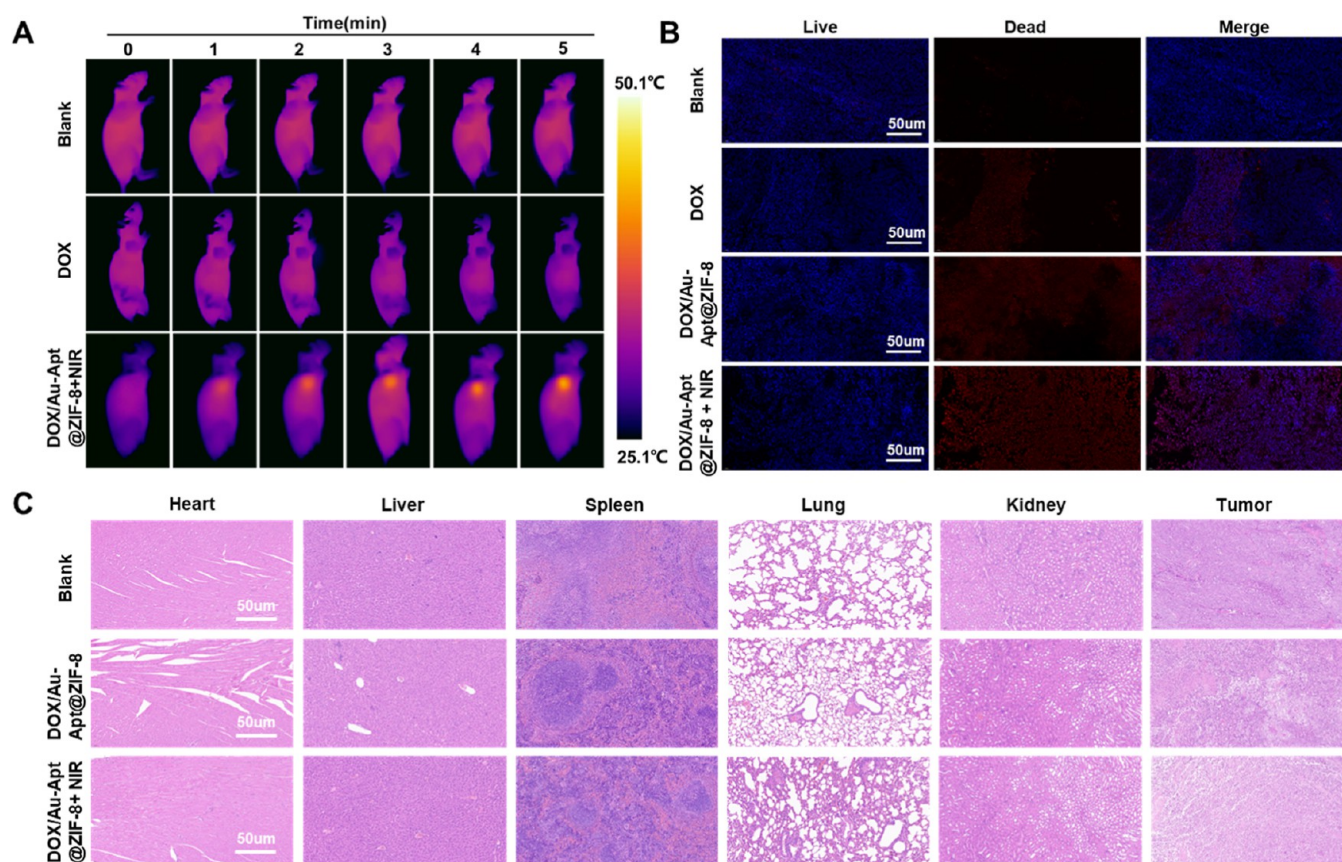


**Figure 6.** (A) Thermal imaging of tumor sites in mice at different treatment times. (B) TUNEL staining of the tumor tissues treated with different drugs. (C) HE staining of each tissue and tumor section. Scale bar: 50  $\mu\text{m}$ .

+ NIR group, which included targeting and PTT. This finding indicated that the ability of the composite nanoparticles to induce tumor cell apoptosis was significantly enhanced and further verified that the nanoparticles exerted dual effects of targeting and photothermal.

**Histological Analysis of Tumor-Bearing Mice.** The aforementioned experimental results revealed that DOX/Au-Apt@ZIF-8 enhanced the targeted antitumor effects. To substantiate that the nanoparticles are nontoxic to the tissues and organs in tumor-bearing mice, HE staining was performed for evaluation. When compared with the blank group, slight morphological changes were observed in the main tissue of mice in each drug treatment group, indicating that DOX/Au-Apt@ZIF-8 had no obvious side effects on the mice (Figure 6C). However, the drug-treated tumor cells exhibited some morphological changes. Cell atypia was obvious, and cell shrinkage was noted. Particularly, a large area of tumor cells in the DOX/Au-Apt@ZIF-8 + NIR group, which received PTT, exhibited morphological changes. These changes further verified the stronger antitumor effects of DOX/Au-Apt@ZIF-8 combined with PTT.

**Effect of Au-Apt@ZIF-8 Nanocarriers on Normal Mice.** To further verify the effect of Au-Apt@ZIF-8 nanocarriers and PTT on mice, weight changes in the mice during treatment were monitored. Moreover, the major organs and viscera of the mice were collected for HE staining. No significant fluctuation was noted in the body weight of the mice in all groups during treatment (Figure S4A). This finding preliminarily indicated that NIR irradiation and Au-Apt@ZIF-8 nanocarriers had no acute side effects on the mice and that they exhibited good

biocompatibility. Histopathological results indicated that no significant changes in the various tissues and organs (Figure S4B), which further implied the good biosafety of nanocores in the mice.

## CONCLUSIONS

In this study, Au NRs were prepared using the seed-mediated growth method. The AS1411 Apt was modified with Au NRs through a coordination bond (Au–S). To prepare DOX/Au-Apt@ZIF-8, DOX and Au-Apt were wrapped with an organic skeleton ZIF-8. DOX/Au-Apt@ZIF-8 offers the advantages of small size, uniform morphology, good dispersibility, and good biocompatibility. Using the dialysis method, the drug release rate was simulated in the pH environment of different parts of the human body. According to the experimental data, DOX/Au-Apt@ZIF-8 has a good drug release rate with a sustained release in an acidic environment. The CCK-8 results revealed that the Au-Apt@ZIF-8 carrier material itself exhibited low toxicity to tumor cells, but, after the drugs were loaded, its ability to inhibit tumor cells was stronger than that of the naked drugs alone. Moreover, the cell cycle was blocked in the S phase. Cell uptake experiments revealed that, as the drug treatment time increased, the fluorescence intensity of the DOX/Au-Apt@ZIF-8 group became higher than that of the DOX group, thereby proving that DOX/Au-Apt@ZIF-8 has a good targeting ability. Furthermore, animal experiments proved that DOX/Au-Apt@ZIF-8 could target tumors by collecting Au NRs that have photothermal effect on tumor cells, thereby increasing the local temperature. Compared with other treatments, DOX/Au-Apt@ZIF-8 + NIR treatment



caused fewer side effects but significantly inhibited tumor growth and induced tumor cell apoptosis. This study thus provides a theoretical and experimental basis for cancer treatment strategies, indicating a good biomedical application prospect for DOX/Au-Apt@ZIF-8.

## ■ ASSOCIATED CONTENT

### SI Supporting Information

The Supporting Information is available free of charge at <https://pubs.acs.org/doi/10.1021/acsanm.4c02074>.

Particle size of Au NRs, Au@ZIF-8, and DOX/Au@ZIF-8, zeta potentials of Au NRs, Au@ZIF-8, and DOX/Au-Apt@ZIF-8, element mapping of DOX/Au-Apt@ZIF-8, heat-up-temperature curve of DOX/Au-Apt@ZIF-8, standard curve of DOX, cumulative release of DOX in the DOX/Au-Apt@ZIF-8 solution at different pH values, changes in particle size of DOX/Au-Apt@ZIF-8 in PBS and DMEM for 7 days, different concentrations of DOX/Au-Apt@ZIF-8 with the blood of mice were incubated with different time of the hemolysis rate, effect of Au-Apt@ZIF-8 nanocarriers on normal mice, changes in the body weight of mice during treatment, H&E staining of tissues and organs in PBS, NIR, Au-Apt@ZIF-8, and Au-Apt@ZIF-8 groups, and confocal laser microscopy images of DOX and DOX/Au-Apt@ZIF-8 incubated with ZR-75-1 cells for different time (PDF)

## ■ AUTHOR INFORMATION

### Corresponding Authors

**Weiwei Zhang** – School of Biological and Food Engineering, Anhui Polytechnic University, Wuhu, Anhui 241000, People's Republic of China; [orcid.org/0000-0001-6141-9153](https://orcid.org/0000-0001-6141-9153); Email: <mailto:zwwjcf0908@163.com>

**Fei Ge** – School of Biological and Food Engineering, Anhui Polytechnic University, Wuhu, Anhui 241000, People's Republic of China; [orcid.org/0000-0002-6308-3224](https://orcid.org/0000-0002-6308-3224); Email: [mailto:gerrylin@126.com](mailto:mailto:gerrylin@126.com)

**Lin Gui** – Department of Microbiology and Immunology, Wannan Medical College, Wuhu, Anhui 241002, People's Republic of China; Email: [mailto:guilin729@126.com](mailto:mailto:guilin729@126.com)

### Authors

**Ting Fang** – Department of Microbiology and Immunology, Wannan Medical College, Wuhu, Anhui 241002, People's Republic of China; [orcid.org/0009-0009-8287-8194](https://orcid.org/0009-0009-8287-8194)

**Zihao Duan** – Department of Microbiology and Immunology, Wannan Medical College, Wuhu, Anhui 241002, People's Republic of China

**Nan Wan** – Department of Microbiology and Immunology, Wannan Medical College, Wuhu, Anhui 241002, People's Republic of China

**Xiaoxuan Zuo** – Department of Microbiology and Immunology, Wannan Medical College, Wuhu, Anhui 241002, People's Republic of China

**Zhongwu Pan** – Department of Microbiology and Immunology, Wannan Medical College, Wuhu, Anhui 241002, People's Republic of China

Complete contact information is available at:

<https://pubs.acs.org/doi/10.1021/acsanm.4c02074>

### Notes

The authors declare no competing financial interest.

## ■ ACKNOWLEDGMENTS

This work was supported by Youth Key Talents Program of Wannan Medical College (wyqnyx202005), Key Project Research Fund of Wannan Medical College (WK2022Z06), Key Research and Development Program of the Anhui Science and Technology Department (2022i01020002 and 202204c06020073), and the Scientific Research Project of Anhui Polytechnic University (Xjky2022089).

## ■ REFERENCES

- (1) Sung, H.; Ferlay, J.; Siegel, R. L.; Laversanne, M.; Soerjomataram, I.; Jemal, A.; Bray, F. Global Cancer Statistics 2020: GLOBOCAN Estimates of Incidence and Mortality Worldwide for 36 Cancers in 185 Countries. *CA A Cancer J. Clin.* **2021**, *71* (3), 209–249.
- (2) Yang, H.; Xu, F.; Chen, Y.; Tian, Z. Structural N-Glycoproteomics Characterization of Cell-Surface N-Glycosylation of MCF-7/ADR Cancer Stem Cells. *J. Chromatogr. B* **2023**, *1219*, 123647.
- (3) Ghahremani, F.; Shahbazi-Gahrouei, D.; Kefayat, A.; Motaghi, H.; Mehrgardi, M. A.; Javanmard, S. H. AS1411 Aptamer Conjugated Gold Nanoclusters as a Targeted Radiosensitizer for Megavoltage Radiation Therapy of 4T1 Breast Cancer Cells. *RSC Adv.* **2018**, *8* (8), 4249–4258.
- (4) Serda, M.; Malarz, K.; Korzuch, J.; Szubka, M.; Zubko, M.; Musiol, R. *In Situ* Cellular Localization of Nonfluorescent [60]-Fullerene Nanomaterial in MCF-7 Breast Cancer Cells. *ACS Biomater. Sci. Eng.* **2022**, *8* (8), 3450–3462.
- (5) Sarhangi, N.; Hajjari, S.; Heydari, S. F.; Ganjizadeh, M.; Rouhollah, F.; Hasanzad, M. Breast Cancer in the Era of Precision Medicine. *Mol. Biol. Rep.* **2022**, *49* (10), 10023–10037.
- (6) Ge, F.; Qiao, Q.; Zhu, L.; Li, W.; Song, P.; Zhu, L.; Tao, Y.; Gui, L. Preparation of a Tumor-Targeted Drug-Loading Material, Amphiphilic Peptide P10, and Analysis of Its Anti-Tumor Activity. *J. Mater. Sci.: Mater. Med.* **2019**, *30* (1), 3.
- (7) Sherlock, S. P.; Tabakman, S. M.; Xie, L.; Dai, H. Photothermally Enhanced Drug Delivery by Ultrasmall Multifunctional FeCo/Graphitic Shell Nanocrystals. *ACS Nano* **2011**, *5* (2), 1505–1512.
- (8) Zhou, Y.; Zhang, C.; Wang, Y.; Zhang, J.; Yan, X.; You, S.; Qi, W.; Su, R.; He, Z. The Safe Laccase@ZIF-8-Prodrug System with GSH Redox Cycle for Effective Targeted Cancer Therapy with Low off-Target Toxicity. *Colloids Surf. B* **2022**, *220*, 112853.
- (9) Park, K. S.; Ni, Z.; Côté, A. P.; Choi, J. Y.; Huang, R.; Uribe-Romo, F. J.; Chae, H. K.; O'Keeffe, M.; Yaghi, O. M. Exceptional Chemical and Thermal Stability of Zeolitic Imidazolate Frameworks. *Proc. Natl. Acad. Sci. U.S.A.* **2006**, *103* (27), 10186–10191.
- (10) Wang, Q.; Sun, Y.; Li, S.; Zhang, P.; Yao, Q. Synthesis and Modification of ZIF-8 and Its Application in Drug Delivery and Tumor Therapy. *RSC Adv.* **2020**, *10* (62), 37600–37620.
- (11) Qian, Z.; Zhao, N.; Wang, C.; Yuan, W. Injectable Self-Healing Polysaccharide Hydrogel Loading CuS and pH-Responsive DOX@ZIF-8 Nanoparticles for Synergistic Photothermal-Photodynamic-Chemo Therapy of Cancer. *J. Mater. Sci. Technol.* **2022**, *127*, 245–255.
- (12) Peng, L.; Qiu, J.; Liu, L.; Li, X.; Liu, X.; Zhang, Y. Preparation of PEG/ZIF-8@HF Drug Delivery System for Melanoma Treatment via Oral Administration. *Drug Delivery* **2022**, *29* (1), 1075–1085.
- (13) Leitner, N. S.; Schroffenegger, M.; Reimhult, E. Polymer Brush-Grafted Nanoparticles Preferentially Interact with Oponins and Albumin. *ACS Appl. Bio Mater.* **2021**, *4* (1), 795–806.
- (14) Lahooti, B.; Akwii, R. G.; Zahra, F. T.; Sajib, M. S.; Lamprou, M.; Alobaida, A.; Lionakis, M. S.; Mattheolabakis, G.; Mikelis, C. M. Targeting Endothelial Permeability in the EPR Effect. *J. Controlled Release* **2023**, *361*, 212–235.
- (15) Ouyang, F.; Zhao, L.; Shuai, Q. Photothermally Driven Degradable Nanomissile for Single-Wavelength Phototherapy and



- Hypoxia-Activated Chemotherapy. *Inorg. Chem. Commun.* **2023**, *157*, 111310.
- (16) Graf, N.; Bielenberg, D. R.; Kolishetti, N.; Muus, C.; Banyard, J.; Farokhzad, O. C.; Lippard, S. J.  $\alpha_v\beta_3$  Integrin-Targeted PLGA-PEG Nanoparticles for Enhanced Anti-Tumor Efficacy of a Pt(IV) Prodrug. *ACS Nano* **2012**, *6* (5), 4530–4539.
- (17) Mehrnia, S. S.; Hashemi, B.; Mowla, S. J.; Nikkhab, M.; Arbabi, A. Radiosensitization of Breast Cancer Cells Using AS1411 Aptamer-Conjugated Gold Nanoparticles. *Radiat. Oncol.* **2021**, *16* (1), 33.
- (18) Kabirian-Dehkordi, S.; Chalabi-Dchar, M.; Mertani, H. C.; Le Guellec, D.; Verrier, B.; Diaz, J.-J.; Mehrgardi, M. A.; Bouvet, P. AS1411-Conjugated Gold Nanoparticles Affect Cell Proliferation through a Mechanism That Seems Independent of Nucleolin. *Nanomed. Nanotechnol. Biol. Med.* **2019**, *21*, 102060.
- (19) Ghahremani, F.; Kefayat, A.; Shahbazi-Gahrouei, D.; Motaghi, H.; Mehrgardi, M. A.; Haghighi-Javanmard, S. AS1411 Aptamer-Targeted Gold Nanoclusters Effect on the Enhancement of Radiation Therapy Efficacy in Breast Tumor-Bearing Mice. *Nanomedicine* **2018**, *13* (20), 2563–2578.
- (20) Kardani, A.; Yaghoobi, H.; Alibakhshi, A.; Khatami, M. Inhibition of miR-155 in MCF-7 Breast Cancer Cell Line by Gold Nanoparticles Functionalized with Antagomir and AS1411 Aptamer. *J. Cell. Physiol.* **2020**, *235* (10), 6887–6895.
- (21) Zhang, Y.; Tan, J.; Zhou, L.; Shan, X.; Liu, J.; Ma, Y. Synthesis and Application of AS1411-Functionalized Gold Nanoparticles for Targeted Therapy of Gastric Cancer. *ACS Omega* **2020**, *5* (48), 31227–31233.
- (22) Grabowska-Jadach, I.; Kalinowska, D.; Drozd, M.; Pietrzak, M. Synthesis, Characterization and Application of Plasmonic Hollow Gold Nanoshells in a Photothermal Therapy—New Particles for Theranostics. *Biomed. Pharmacother.* **2019**, *111*, 1147–1155.
- (23) Khatami, F.; Matin, M. M.; Danesh, N. M.; Bahrami, A. R.; Abnous, K.; Taghdisi, S. M. Targeted Delivery System Using Silica Nanoparticles Coated with Chitosan and AS1411 for Combination Therapy of Doxorubicin and anti-miR-21. *Carbohydr. Polym.* **2021**, *266*, 118111.
- (24) Yaghoobi, E.; Shojaei, S.; Ramezani, M.; Alibolandi, M.; Charbgo, F.; Nameghi, M. A.; Khatami, F.; Ashjaei, M. S.; Abnous, K.; Taghdisi, S. M. A Novel Targeted Co-Delivery System for Transfer of Epirubicin and anti-miR-10b into Cancer Cells through a Linear DNA Nanostructure Consisting of FOXM1 and AS1411 Aptamers. *J. Drug Delivery Sci. Technol.* **2021**, *63*, 102521.
- (25) Meng, Z.; Liu, Y.; Xu, K.; Sun, X.; Yu, Q.; Wu, Z.; Zhao, Z. Biomimetic Polydopamine-Modified Silk Fibroin/Curcumin Nanofibrous Scaffolds for Chemo-Photothermal Therapy of Bone Tumor. *ACS Omega* **2021**, *6* (34), 22213–22223.
- (26) Yang, L.; Tseng, Y.-T.; Suo, G.; Chen, L.; Yu, J.; Chiu, W.-J.; Huang, C.-C.; Lin, C.-H. Photothermal Therapeutic Response of Cancer Cells to Aptamer-Gold Nanoparticle-Hybridized Graphene Oxide under NIR Illumination. *ACS Appl. Mater. Interfaces* **2015**, *7* (9), 5097–5106.
- (27) Bhole, R. A Comprehensive Review on Photodynamic Therapy (PDT) and Photothermal Therapy (PTT) for Cancer Treatment. *Turk. J. Oncol.* **2021**, *36* (1), 125–132.
- (28) Zhang, W.; Ding, M.; Zhang, H.; Shang, H.; Zhang, A. Tumor Acidity and Near-Infrared Light Responsive Drug Delivery MoS<sub>2</sub>-Based Nanoparticles for Chemo-Photothermal Therapy. *Photodiagnosis Photodyn. Ther.* **2022**, *38*, 102716.
- (29) Pham, T.-T. D.; Phan, L. M. T.; Cho, S.; Park, J. Enhancement Approaches for Photothermal Conversion of Donor-Acceptor Conjugated Polymer for Photothermal Therapy: A Review. *Sci. Technol. Adv. Mater.* **2022**, *23* (1), 707–734.
- (30) Yang, L.; Tseng, Y.-T.; Suo, G.; Chen, L.; Yu, J.; Chiu, W.-J.; Huang, C.-C.; Lin, C.-H. Photothermal Therapeutic Response of Cancer Cells to Aptamer-Gold Nanoparticle-Hybridized Graphene Oxide under NIR Illumination. *ACS Appl. Mater. Interfaces* **2015**, *7* (9), 5097–5106.
- (31) Yue, H.; Yuan, L.; Zhang, W.; Zhang, S.; Wei, W.; Ma, G. Macrophage Responses to the Physical Burden of Cell-Sized Particles. *J. Mater. Chem. B* **2018**, *6* (3), 393–400.
- (32) Zheng, M.; Zhao, P.; Luo, Z.; Gong, P.; Gao, G.; Sheng, Z.; Zheng, C.; Chen, C.; Ma, Y.; Cai, L. Remote and Noninvasive NIR-Triggered DOX Release from DOX/ICG-Loaded Temperature-Responsive Nanoparticles to Promote Anti-Tumor Effect. *Nanomed. Nanotechnol. Biol. Med.* **2016**, *12* (2), 547.
- (33) Jiapaer, Z.; Zhang, L.; Ma, W.; Liu, H.; Li, C.; Huang, W.; Shao, S. Disulfiram-Loaded Hollow Copper Sulfide Nanoparticles Show Anti-Tumor Effects in Preclinical Models of Colorectal Cancer. *Biochem. Biophys. Res. Commun.* **2022**, *635*, 291–298.
- (34) Kultravut, K.; Kuboyama, K.; Sedlarik, V.; Mrlik, M.; Osicka, J.; Dröhsler, P.; Ougizawa, T. Localization of Poly(Glycidyl Methacrylate) Grafted on Reduced Graphene Oxide in Poly(Lactic Acid)/Poly(Trimethylene Terephthalate) Blends for Composites with Enhanced Electrical and Thermal Conductivities. *ACS Appl. Nano Mater.* **2021**, *4* (8), 8511–8519.
- (35) Xia, H.; Zhu, J.; Men, C.; Wang, A.; Mao, Q.; Feng, Y.; Li, J.; Xu, J.; Cheng, X.; Shi, H. Light-Initiated Aggregation of Gold Nanoparticles for Synergistic Chemo-Photothermal Tumor Therapy. *Nanoscale Adv.* **2023**, *5* (11), 3053–3062.
- (36) Fang, X.; Lui, K.-H.; Li, S.; Lo, W.-S.; Li, X.; Gu, Y.; Wong, W. Multifunctional Nanotheranostic Gold Nanocage/Selenium Core-Shell for PAI-Guided Chemo-Photothermal Synergistic Therapy in Vivo. *Int. J. Nanomed.* **2020**, *15*, 10271–10284.
- (37) Hao, W. U.; Shan, X. J.; Hong, L. Y.; Han, W. X.; Wei, H.; Die, L. M.; Qiang, S.; Bin, G. Tetrahedral DNA Nanostructure-Modified Gold Nanorod-Based Anticancer Nanomaterials for Combined Photothermal Therapy and Chemotherapy. *Biomed. Environ. Sci.* **2022**, *35* (12), 1115–1125.
- (38) Jiang, P.; Hu, Y.; Li, G. Biocompatible Au@Ag nanorod@ZIF-8 Core-Shell Nanoparticles for Surface-Enhanced Raman Scattering Imaging and Drug Delivery. *Talanta* **2019**, *200*, 212–217.
- (39) Zhang, W.; Ding, X.; Cheng, H.; Yin, C.; Yan, J.; Mou, Z.; Wang, W.; Cui, D.; Fan, C.; Sun, D. Dual-Targeted Gold Nanoprisms for Recognition of Early Apoptosis, Dual-Model Imaging and Precise Cancer Photothermal Therapy. *Theranostics* **2019**, *9* (19), 5610–5625.
- (40) Chen, Q.-Q.; Hou, R.-N.; Zhu, Y.-Z.; Wang, X.-T.; Zhang, H.; Zhang, Y.-J.; Zhang, L.; Tian, Z.-Q.; Li, J.-F. Au@ZIF-8 Core-Shell Nanoparticles as a SERS Substrate for Volatile Organic Compound Gas Detection. *Anal. Chem.* **2021**, *93* (19), 7188–7195.
- (41) Almada, M.; Leal-Martínez, B.; Hassan, N.; Kogan, M. J.; Burboa, M. G.; Topete, A.; Valdez, M. A.; Juárez, J. Photothermal Conversion Efficiency and Cytotoxic Effect of Gold Nanorods Stabilized with Chitosan, Alginate and Poly(Vinyl Alcohol). *Mater. Sci. Eng., C* **2017**, *77*, 583–593.
- (42) Meng, Y.; Wang, S.; Li, C.; Qian, M.; Zheng, Y.; Yan, X.; Huang, R. TKD Peptide as a Ligand Targeting Drug Delivery Systems to memHsp70-Positive Breast Cancer. *Int. J. Pharm.* **2016**, *498* (1–2), 40–48.
- (43) Pahore, A. K.; Khan, S.; Karim, N. Anticancer Effect of Illicium Verum (Star Anise Fruit) against Human Breast Cancer MCF-7 Cell Line. *Pak. J. Med. Sci.* **2023**, *39* (1), 70–74.
- (44) Mittal, A.; Gandhi, S.; Roy, I. Mechanistic Interaction Studies of Synthesized ZIF-8 Nanoparticles with Bovine Serum Albumin Using Spectroscopic and Molecular Docking Approaches. *Sci. Rep.* **2022**, *12* (1), 10331.
- (45) Yang, X.; Song, T.; Su, T.; Hu, J.; Wu, S. Exploring the Influence of the Reused Methanol Solution for the Structure and Properties of the Synthesized ZIF-8. *Processes* **2022**, *10* (9), 1705.
- (46) Wang, M.; Li, F.; Lu, T.; Wu, R.; Yang, S.; Chen, W. Photodynamic and Ferroptotic Ce6@ZIF-8@ssPDA for Head and Neck Cancer Treatment. *Mater. Des.* **2022**, *224*, 111403.
- (47) Song, L.; Liu, L.; Zhu, M.; Dai, B. Process Monitoring of the Au-S Bond Conversion in Acetylene Hydrochlorination. *Chin. J. Chem. Eng.* **2022**, *45*, 32–40.

- (48) Chen, M.-M.; Hao, H.-L.; Zhao, W.; Zhao, X.; Chen, H.-Y.; Xu, J.-J. A Plasmon-Enhanced Theranostic Nanoplatform for Synergistic Chemo-Phototherapy of Hypoxic Tumors in the NIR-II Window. *Chem. Sci.* **2021**, *12* (32), 10848–10854.
- (49) Huang, J.; Xu, Z.; Jiang, Y.; Law, W.; Dong, B.; Zeng, X.; Ma, M.; Xu, G.; Zou, J.; Yang, C. Metal Organic Framework-Coated Gold Nanorod as an on-Demand Drug Delivery Platform for Chemo-Photothermal Cancer Therapy. *J. Nanobiotechnol.* **2021**, *19* (1), 219.
- (50) Mamnoon, B.; Loganathan, J.; Confeld, M. I.; De Fonseca, N.; Feng, L.; Froberg, J.; Choi, Y.; Tuvin, D. M.; Sathish, V.; Mallik, S. Targeted Polymeric Nanoparticles for Drug Delivery to Hypoxic, Triple-Negative Breast Tumors. *ACS Appl. Bio Mater.* **2021**, *4* (2), 1450–1460.
- (51) Fu, Y.; Xin, M.; Chong, J.; Li, R.; Huang, M. Plasmonic Gold nanostars@ZIF-8 Nanocomposite for the Ultrasensitive Detection of Gaseous Formaldehyde. *J. Mater. Sci.* **2021**, *56* (6), 4151–4160.
- (52) Bae, C.; Lee, J.; Yao, L.; Park, S.; Lee, Y.; Lee, J.; Chen, Q.; Kim, J. Mechanistic Insight into Gold Nanorod Transformation in Nanoscale Confinement of ZIF-8. *Nano Res.* **2021**, *14* (1), 66–73.
- (53) Tian, F.; Zhang, H.; Liu, S.; Wu, T.; Yu, J.; Wang, D.; Jin, X.; Peng, C. Visible-Light-Driven CO<sub>2</sub> Reduction to Ethylene on CdS: Enabled by Structural Relaxation-Induced Intermediate Dimerization and Enhanced by ZIF-8 Coating. *Appl. Catal., B* **2021**, *285*, 119834.
- (54) Feng, Y.; Xu, Y.; Wen, Z.; Ning, X.; Wang, J.; Wang, D.; Cao, J.; Zhou, X. Cerium End-Deposited Gold Nanorods-Based Photo-immunotherapy for Boosting Tumor Immunogenicity. *Pharmaceutics* **2023**, *15* (4), 1309.
- (55) Schuh, E. M.; Portela, R.; Gardner, H. L.; Schoen, C.; London, C. A. Safety and Efficacy of Targeted Hyperthermia Treatment Utilizing Gold Nanorod Therapy in Spontaneous Canine Neoplasia. *BMC Vet. Res.* **2017**, *13* (1), 294.
- (56) Fu, Z.; Williams, G. R.; Niu, S.; Wu, J.; Gao, F.; Zhang, X.; Yang, Y.; Li, Y.; Zhu, L.-M. Functionalized Boron Nanosheets as an Intelligent Nanoplatform for Synergistic Low-Temperature Photothermal Therapy and Chemotherapy. *Nanoscale* **2020**, *12* (27), 14739–14750.
- (57) Tun, J. O.; Salvador-Reyes, L. A.; Velarde, M. C.; Saito, N.; Suwanborirux, K.; Concepcion, G. P. Synergistic Cytotoxicity of Renieramycin M and Doxorubicin in MCF-7 Breast Cancer Cells. *Mar. Drugs* **2019**, *17* (9), 536.
- (58) Chen, Y.; Shi, S.; Dai, Y. Research Progress of Therapeutic Drugs for Doxorubicin-Induced Cardiomyopathy. *Biomed. Pharmacother.* **2022**, *156*, 113903.
- (59) Cortés-Funes, H.; Coronado, C. Role of Anthracyclines in the Era of Targeted Therapy. *Cardiovasc. Toxicol.* **2007**, *7* (2), 56–60.
- (60) Zhao, X.; Qi, T.; Kong, C.; Hao, M.; Wang, Y.; Li, J.; Liu, B.; Gao, Y.; Jiang, J. Photothermal Exposure of Polydopamine-Coated Branched Au–Ag Nanoparticles Induces Cell Cycle Arrest, Apoptosis, and Autophagy in Human Bladder Cancer Cells. *Int. J. Nanomed.* **2018**, *13*, 6413–6428.